

Theoretical predictions of experimental observables sensitive to the symmetry energy

Results of the SMF transport model

Maria Colonna¹, Virgil Baran² and Massimo Di Toro^{1,3}

¹ Laboratori Nazionali del Sud, INFN, via Santa Sofia 62, I-95123, Catania, Italy

² Physics Faculty, University of Bucharest, Romania

³ Physics-Astronomy Dept., University of Catania, Italy

Received: date / Revised version: date

Abstract. In the framework of mean-field based transport approaches, we discuss recent results concerning heavy ion reactions between charge asymmetric systems, from low up to intermediate energies. We focus on isospin sensitive observables, aiming at extracting information on the density dependence of the isovector part of the nuclear effective interaction and of the nuclear symmetry energy. For reactions close to the Coulomb barrier, we explore the structure of collective dipole oscillations, rather sensitive to the low-density behavior of the symmetry energy. In the Fermi energy regime, we investigate the interplay between dissipation mechanisms, fragmentation and isospin effects. At intermediate energies, where regions with higher density and momentum are reached, we discuss collective flows and their sensitivity to the momentum dependence of the isovector interaction channel, which determines the splitting of neutron and proton effective masses. Finally, we also discuss the isospin effect on the possible phase transition from nucleonic matter to quark matter. Results are critically reviewed, also trying to establish a link, when possible, with the outcome of other transport models.

PACS. 25.70.-z Low and intermediate energy heavy-ion reactions – 24.60.Ky Fluctuation phenomena

1 Introduction

The behavior of nuclear matter in several conditions of density, temperature and N/Z asymmetry is of fundamental importance for the understanding of many phenomena involving nuclear systems and astrophysical compact objects. This information can be accessed by mean of heavy ion collision experiments, where transient states of nuclear matter spanning a large variety of regimes can be created. Actually this study allows one to learn about the corresponding behavior of the nuclear effective interaction, which provides the nuclear Equation of State (EOS) in the equilibrium limit. Over the past years, measurements of experimental observables, like isoscalar collective vibrations, collective flows and meson production, have contributed to constrain the EOS of symmetric matter for densities up to five time the saturation value [1]. More recently, the availability of exotic beams has made it possible to explore, in laboratory conditions, new aspects of nuclear structure and dynamics up to extreme ratios of neutron (N) to proton (Z) numbers, also opening the way to the investigation of the EOS of asymmetric matter, which has few experimental constraints. Indeed, the isovector part of the nuclear effective interaction and the corresponding

symmetry energy of the EOS (Asy-EOS) are largely unknown as soon as we move away from normal density.

Nevertheless, this information is essential in the astrophysical context, for the understanding of the properties of compact objects such as neutron stars, whose crust behaves as low-density asymmetric nuclear matter [2] and whose core may touch extreme values of density and asymmetry. Moreover, the low-density behavior of the symmetry energy also affects the structure of exotic nuclei and the appearance of new features involving the neutron skin, which are currently under intense investigation. [3].

Over the past years, several observables which are sensitive to the Asy-EOS and testable experimentally, have been suggested [4, 5, 6, 7]. In this article we will review recent results on dissipative collisions in a wide range of beam energies, from just above the Coulomb barrier up to the AGeV range, on the basis of transport theories of the Stochastic Mean Field (SMF) type. Low to Fermi energies will bring information on the symmetry term around (below) normal density, while intermediate energies will probe high density regions.

2 Transport theories and symmetry energy

Nuclear reactions are modeled by solving transport equations based on mean field theories, with short range (2p-2h) correlations included via hard nucleon-nucleon elastic collisions and via stochastic forces, selfconsistently evaluated from the mean phase-space trajectory, see [8,5]. Stochasticity is essential in order to get distributions as well as to allow for the growth of dynamical instabilities.

In the energy range up to a few hundred $AMeV$, the appropriate tool is the so-called Boltzmann-Langevin (BL) equation [8]:

$$\frac{df}{dt} = \frac{\partial f}{\partial t} + \{f, H\} = I_{coll}[f] + \delta I[f], \quad (1)$$

where $f(\mathbf{r}, \mathbf{p}, t)$ is the one-body distribution function, the semi-classical analog of the Wigner transform of the one-body density matrix, $H(\mathbf{r}, \mathbf{p}, t)$ the mean field Hamiltonian, I_{coll} the two-body collision term incorporating the Fermi statistics of the particles, and $\delta I[f]$ its fluctuating part. Here we follow the approximate treatment of the BLE introduced in Ref.[9], the Stochastic Mean Field (SMF) model. The numerical procedure to integrate the transport equations is based on the test-particle method.

Effective interactions (associated with a given EOS) can be considered as an input of the transport code and from the comparison with experimental data one can finally get some hints on nuclear matter properties.

We recall that the symmetry energy E_{sym} appears in the energy density functional $\epsilon(\rho, \rho_i) \equiv \epsilon(\rho) + \rho \frac{E_{sym}}{A} (\rho_i/\rho)^2 + O(\rho_i/\rho)^4 + \dots$, expressed in terms of total ($\rho = \rho_p + \rho_n$) and isospin ($\rho_i = \rho_p - \rho_n$) densities. E_{sym} gets a kinetic contribution directly from basic Pauli correlations and a potential part, $C(\rho)$, from the highly controversial isospin dependence of the effective interactions:

$$\frac{E_{sym}}{A} = \frac{E_{sym}}{A}(kin) + \frac{E_{sym}}{A}(pot) \equiv \frac{\epsilon_F}{3} + \frac{C(\rho)}{2\rho_0}\rho \quad (2)$$

(ρ_0 denotes the saturation density). The nuclear mean-field, consistently derived from the energy functional, can be written as:

$$U_q = A \frac{\rho}{\rho_0} + B \left(\frac{\rho}{\rho_0}\right)^{\alpha+1} + C(\rho) \frac{\rho_n - \rho_p}{\rho_0} \tau_q + \frac{1}{2} \frac{\partial C}{\partial \rho} \frac{(\rho_n - \rho_p)^2}{\rho_0}, \quad (3)$$

where $\tau_q = +1(-1)$ for $q = n(p)$. The isoscalar section is fixed requiring that the saturation properties of symmetric nuclear matter, with a compressibility modulus around $K = 200 MeV$, are reproduced (which corresponds to the Skyrme SKM* effective interaction). The corresponding values of the coefficients are $A = -356.8 MeV$, $B = 303.9 MeV$, $\alpha = 1/6$.

The sensitivity of the simulation results is tested against different choices of the density dependence of the isovector part of the effective interaction. We employ three different parameterizations of $C(\rho)$: the asysoft, the asystiff and asysuperstiff respectively, see [5] for a detailed description. The value of the symmetry energy, E_{sym}/A , at saturation,

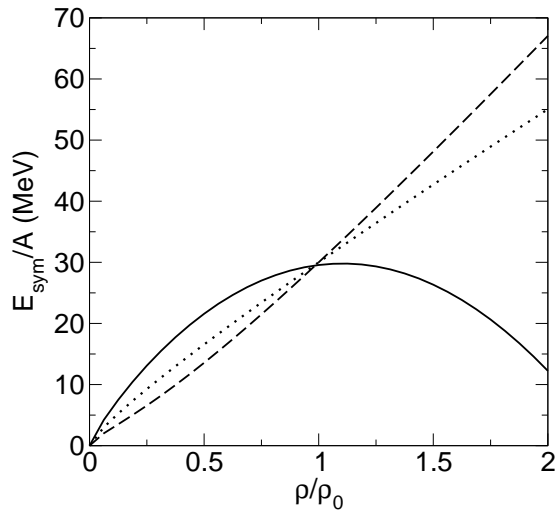


Fig. 1. Three effective parameterizations of the symmetry energy : asystiff (dotted line), asysoft (full line) and asysuperstiff (dashed line).

as well as the slope parameter, $L = 3\rho_0 \frac{dE_{sym}/A}{d\rho} |_{\rho=\rho_0}$, are reported in Table 1 (first two columns) for each of these Asy-EOS. Just below the saturation density the asysoft mean field has a weak variation with density while the asysuperstiff shows a rapid decrease, see figure 1.

For protons, the Coulomb interaction is also included in the simulations.

Surface terms are not explicitly included in the mean-field potential, however surface effects are accounted for by considering finite width wave packets for the test particles employed in the numerical resolution of Eq.(1). The width is tuned to reproduce the surface energy of nuclei in the ground state [10]. This method also induces the presence of a surface term in the symmetry energy. We have checked that properties connected to surface effects, such as the neutron skin of neutron-rich nuclei, are in reasonable agreement with calculations of other models employing similar interactions [11,12].

Momentum-dependent effective interactions may also be implemented into Eq.(1) and will be considered in the following for the study of observables which are particularly sensitive to this ingredient. In particular, we will discuss results related to the momentum dependence of the isovector channel of the interaction, leading to the splitting of neutron and proton effective masses (see Section 5).

3 Collective excitations in neutron-rich systems

One of the important tasks in many-body physics is to understand the emergence of collective features as well as their structure in terms of the individual motion of the constituents. The experimental characterization and

theoretical description of collective excitations appearing in charge asymmetric and exotic systems is a challenge for modern nuclear physics.

3.1 New exotic collective excitations

Recent experiments have provided several evidences about the existence of new collective excitations in neutron-rich systems, but the available information is still incomplete and their nature is a matter of debate. In particular, many efforts have been devoted to the study of the Pygmy Dipole Resonance (PDR), identified as an unusually large concentration of the dipole response at energies below the values corresponding to the Giant Dipole Resonance (GDR). The latter is one of the most prominent and robust collective motions, present in all nuclei, whose centroid position varies, for medium-heavy nuclei, as $80A^{-1/3} MeV$. From a comparison of the available data for stable and unstable Sn isotopes a correlation between the fraction of pygmy strength and isospin asymmetry was noted [13]. In general the exhausted sum-rule increases with the proton-to-neutron asymmetry. This behavior was related to the symmetry energy properties below saturation and therefore connected to the size of the neutron skin [14, 15, 3].

In spite of the theoretical progress in the interpretation of this mode and new experimental information [16, 17, 18, 19], a number of critical questions concerning the nature of the PDR still remains. Here we want to address the important issue related to the collective nature of the PDR in connection with the role of the symmetry energy.

A microscopic, self-consistent study of the collective features and of the role of the nuclear effective interaction upon the PDR can be performed within the Landau theory of Fermi liquids. This is based on two coupled Vlasov kinetic equations (see Eq.(1), neglecting two-body correlations) for neutron and proton one-body distribution functions $f_q(\mathbf{r}, \mathbf{p}, t)$ with $q = n, p$, and was applied quite successfully in describing various features of the GDR, including pre-equilibrium dipole excitation in fusion reactions [20], see Subsection 3.4. However, it should be noticed that within such a semi-classical description shell effects are absent, certainly important in shaping the fine structure of the dipole response [21]. By solving numerically the Vlasov equation, in the absence of Coulomb interaction, Urban [22] evidenced from the study of the total dipole moment D a collective response around $8.6 MeV$ which was identified as a pygmy mode. It was pointed out, from the properties of transition densities and velocities, that the PDR can be related to one of the low-lying modes associated with isoscalar toroidal excitations, providing indications about its isoscalar character. Here, considering in the transport simulations also the Coulomb interaction, we can investigate in a complementary way the collective nature of the PDR by studying the dynamics of the pygmy degree of freedom, that is usually associated with the neutron excess in the nuclear surface [11]. Moreover, we can explore the isoscalar character of the mode by a comparative analysis employing three different density parametrizations of the symmetry energy.

3.2 Ingredients of the simulations

We consider the neutron rich nucleus ^{132}Sn and we determine its ground state configuration as the equilibrium (static) solution of Eq.(1). Then proton and neutron densities $\rho_q(\mathbf{r}, t) = \int \frac{2d^3\mathbf{p}}{(2\pi\hbar)^3} f_q(\mathbf{r}, \mathbf{p}, t)$ can be evaluated. As an additional check of our initialization procedure, the neutron and proton mean square radii

$$\langle r_q^2 \rangle = \frac{1}{N_q} \int r^2 \rho_q(\mathbf{r}, t) d^3\mathbf{r}, \quad (4)$$

as well as the skin thickness $\Delta R_{np} = \sqrt{\langle r_n^2 \rangle} - \sqrt{\langle r_p^2 \rangle}$, were also calculated in the ground state and shown in Table 1.

The values obtained with the semi-classical approach are in a reasonable agreement with those reported by employing other models for similar interactions [12]. The neutron skin thickness is increasing with the slope parameter, as expected from a faster reduction of the symmetry term on the surface [14, 5]. This feature has been discussed in detail in [3].

To mimic the excitation induced by nuclear reactions, we introduce an initial perturbation in our system. To inquire on the collective properties of the pygmy dipole, we first boost along the z direction all excess neutrons ($N_e = 32$) and, in opposite direction, all core nucleons, while keeping the c.m. of the nucleus at rest (Pygmy-like initial conditions). The excess neutrons were identified as the most distant $N_e = 32$ neutrons from the nucleus c.m.. Then the system is left to evolve and the evolution of the collective coordinates Y , X_c and X , associated with the different isovector dipole modes (pygmy, core and total dipole) is followed for $600 fm/c$ by solving numerically the equations (1). The total dipole moment D is linked to the dipole D_y and the core dipole D_c by the following relation:

$$\mathbf{D} = \frac{NZ}{A} \mathbf{X} = \frac{Z N_c}{A_c} \mathbf{X}_c + \frac{Z N_e}{A} \mathbf{Y} \equiv \mathbf{D}_c + \mathbf{D}_y, \quad (5)$$

where N_c and A_c denote neutron and mass number of the core, respectively.

3.3 Results for dipole oscillations

In figure 2 we plot the time evolution of D_y , D and D_c , for two Asy-EoS. Apart from the quite undamped oscillations of the Y coordinate, we also remark that the core does not remain inert. Indeed, while D_y approaches its maximum value, an oscillatory motion of the dipole D_c initiates and this response is symmetry energy dependent: the larger is the slope parameter L , the more delayed is the isovector core reaction. This can be explained in terms of low-density (surface) contributions to the vibration and therefore of the density behavior of the symmetry energy below normal density: a larger L corresponds to a larger neutron presence in the surface (see Table I) and so to a smaller coupling to the core protons. We see that the total dipole $D(t)$ is strongly affected by the presence of isovector

asy-EoS	E_{sym}/A	L (MeV)	R_n (fm)	R_p (fm)	ΔR_{np} (fm)
asysoft	29.9	14.4	4.90	4.65	0.25
asystiff	28.3	72.6	4.95	4.65	0.30
asysupstiff	28.3	96.6	4.96	4.65	0.31

Table 1. The symmetry energy at saturation (in MeV), the slope parameters, neutron rms radius, protons rms radius, neutron skin thickness of ^{132}Sn for the three Asy-EOS.

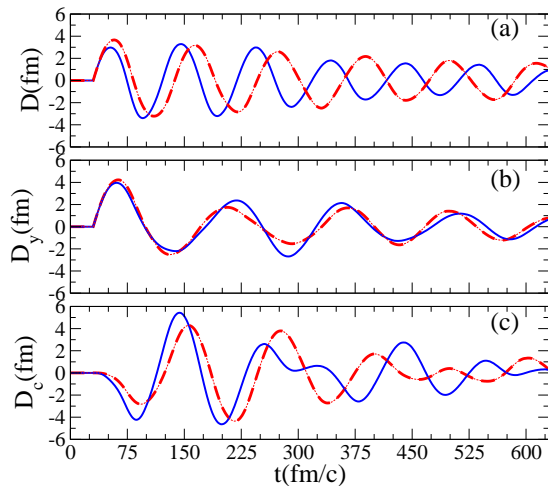


Fig. 2. (Color online) The time evolution of the total dipole D (a), of the dipole D_y (b) and of core dipole D_c (c), for asysoft (the blue (solid) lines) and asysuperstiff (the red (dashed) lines) EOS. Pygmy-like initial excitation [11].

core oscillations, mostly related to the isovector part of the effective interaction. Indeed, $D(t)$ gets a higher oscillation frequency with respect to D_y , sensitive to the Asy-EOS. The fastest vibrations are observed in the asysoft case, which gives the largest value of the symmetry energy below saturation. On the other hand, the frequency of the pygmy mode seems to be not much affected by the trend of the symmetry energy below saturation, see also next figure 3, clearly showing the different nature, isoscalar-like, of this oscillation. For each Asy-EOS we calculate the power spectrum of D_y : $|D_y(\omega)|^2 = \left| \int_{t_0}^{t_{max}} D_y(t) e^{-i\omega t} dt \right|^2$, and similarly for D . The results are shown in figure 3. The position of the centroid corresponding to the GDR shifts toward larger values when we move from asysuperstiff (largest slope parameter L) to asysoft EOS. As it clearly appears from Fig.3 (bottom), the energy centroid associated with the PDR is situated below the GDR peak, at around 8.5MeV , quite insensitive to the Asy-EOS, pointing to an isoscalar-like nature of this mode. Hence the structure of the dipole response can be explained in terms of the development of isoscalar-like (PDR) and isovector-like (GDR) modes [23]. We observe that the GDR energy centroid is underestimated in comparison with experimental data, a fact probably related to the choice of the interaction, which has not an effective mass [24]. On the other hand, the PDR energy centroid looks in better agreement with experimental observations [25]. This may suggest that the PDR peak energy is less affected by the

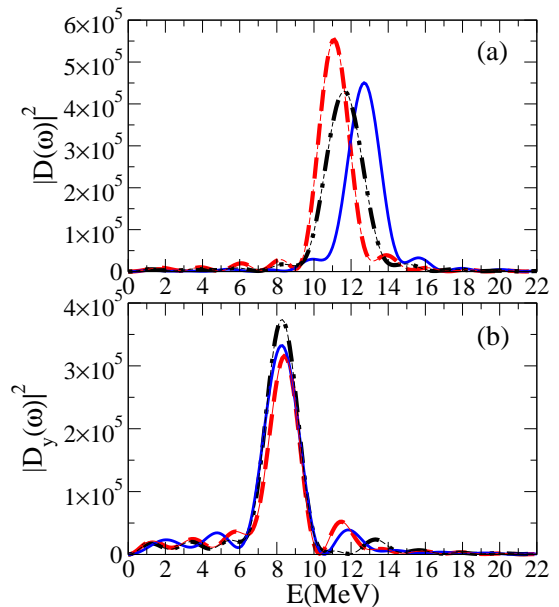


Fig. 3. (Color online) The power spectrum of total dipole (a) and of the dipole D_y (b) (in fm^4/c^2), for asysoft (the blue (solid) lines), asystiff (the black (dot-dashed) lines) and asysuperstiff (the red (dashed) lines) EOS. Pygmy-like initial conditions [11].

momentum dependence of the effective interaction, however more complete analyses should be performed.

Both modes are excited in the considered pygmy-like initial conditions. Looking at the total dipole mode direction, that is close to the isovector-like normal mode, one observes a quite large contribution in the GDR region. On the other hand, although the pygmy mode has a more complicated structure [22], the Y direction appears closely related to it. Indeed, looking at D_y , a larger response amplitude is detected in the pygmy region, see figure 3 (bottom).

The results crucially depend on the initial excitation of the system. Let us consider the case of a GDR-like excitation, corresponding to a boost of all neutrons against all protons, keeping the c.m. at rest. Now the initial conditions favor the isovector-like mode and even in the Y direction we observe a sizable contribution in the GDR region, see the Fourier spectrum of D_y in figure 4. Hence a part of the N_e excess neutrons is involved in a GDR type motion, and the relative weight depends on the symmetry energy: more neutrons are involved in the pygmy mode in the asysuperstiff EOS case, in connection to the larger slope L . We notice that a larger slope L implies a larger coupling between isoscalar and isovector oscillations

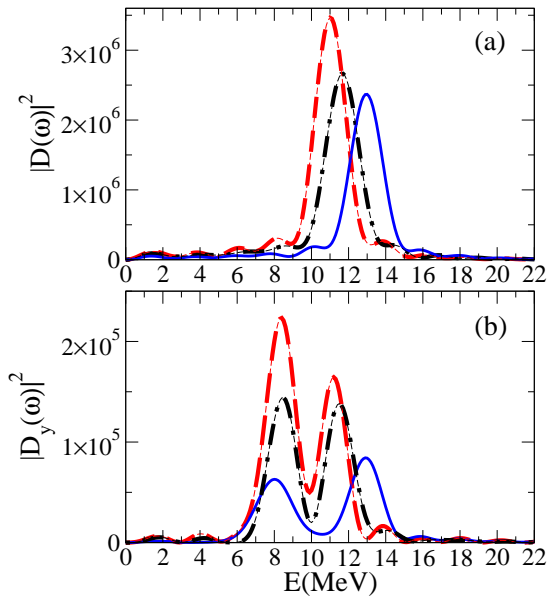


Fig. 4. (Color online) The same as in figure 3 but for a GDR-like initial excitation [11].

in asymmetric matter. As a consequence, even for a GDR-like excitation, the response in the PDR region will be of greater amplitude for a larger L . This is also observed in the Fourier spectrum of the total dipole mode D (figure 4, top). We notice that the strength function is related to $Im(D(\omega))$ [26] and then the corresponding cross section can be calculated. Our estimate of the integrated cross section over the PDR region represents 2.7% for asysoft, 4.4% for asystiff and 4.5% for asysuperstiff, out of the total cross section. We also remark that a larger slope L is associated with a larger neutron skin, thus building a correlation between the energy weighted sum rule (EWSR) exhausted by the PDR and the neutron skin thickness [25], in agreement with the results of [27].

3.4 The prompt dipole γ -ray emission in dissipative collisions

The low-density behavior of the symmetry energy can also be explored looking at pre-equilibrium dipole excitations in dissipative charge asymmetric reactions around 10 $AMeV$. The possibility of an entrance channel bremsstrahlung dipole radiation due to an initial different N/Z distribution was suggested at the beginning of the nineties [28]. After several experimental evidences, in fusion as well as in deep-inelastic reactions, [29,30,31] (and references therein), the process is now well understood and stimulating new perspectives are coming from the use of radioactive beams.

During the charge equilibration process taking place in the first stage of dissipative reactions between colliding ions with different N/Z ratios, a large amplitude dipole collective motion develops in the composite dinuclear system, the so-called Dynamical Dipole mode. This collective dipole gives rise to a prompt γ -ray emission which depends

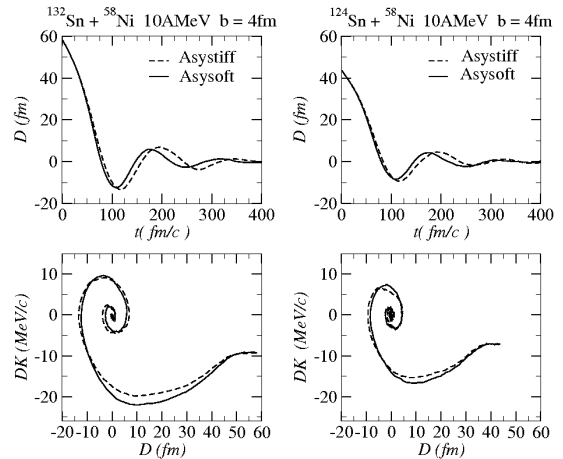


Fig. 5. Dipole Dynamics at 10 $AMeV$, $b = 4fm$ centrality. Left panels: exotic “132” system. Upper panel: time evolution of dipole moment $D(t)$ in coordinate space; Lower panel: dipole phase-space correlation (see text). Right panels: same as before for the stable “124” system. Solid lines correspond to asysoft EOS, the dashed to asystiff EOS [20].

on the absolute value of the initial amplitude, $D(t = 0)$, on the fusion/deep-inelastic dynamics and on the symmetry term, below saturation, that is acting as a restoring force. Indeed this oscillation develops in the low density interface between the two colliding ions (neck region).

A detailed description is obtained in the mean field transport approach [32]. One can follow the time evolution of the dipole moment in the r -space, $D(t) = \frac{NZ}{A}(R_Z - R_N)$ and in p -space, $DK(t) = (\frac{P_p}{Z} - \frac{P_n}{N})$, being R_p , P_p (R_n , P_n) the centers of mass in coordinate and momentum space for protons (neutrons). A nice “spiral-correlation” clearly denotes the collective nature of the mode, see figure 5 for $Sn + Ni$ reactions at 10 MeV/A.

The “prompt” photon emission probability, with energy $E_\gamma = \hbar\omega$, can be estimated applying a bremsstrahlung approach to the dipole evolution given from the BL equation (1):

$$\frac{dP}{dE_\gamma} = \frac{2e^2}{3\pi\hbar c^3 E_\gamma} |D''(\omega)|^2, \quad (6)$$

where $D''(\omega)$ is the Fourier transform of the dipole acceleration $D''(t)$. We remark that in this way it is possible to evaluate, in *absolute* values, the corresponding pre-equilibrium photon emission.

We must add a couple of comments of interest for the experimental selection of the Dynamical Dipole: i) The centroid is always shifted to lower energies (large deformation of the dinucleus); ii) A clear angular anisotropy should be present since the prompt mode has a definite axis of oscillation (on the reaction plane) at variance with the statistical GDR . These features have been observed in recent experiments [30].

The use of unstable neutron rich projectiles would largely increase the effect, due to the possibility of larger entrance channel asymmetries. Indeed one can notice in figure 5 the large amplitude of the first oscillation for the

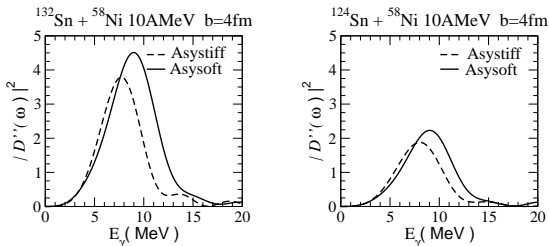


Fig. 6. Left panel: exotic “132” system. Power spectra of the dipole acceleration at $b = 4\text{fm}$ (in c^2 units). Right panel: corresponding results for the stable “124” system. Solid lines correspond to asysoft EOS, the dashed to asystiff EOS [20].

“132” system. We also remark the delayed dynamics for the asystiff EOS related to a weaker isovector restoring force. In figure 6 (left panel) we report the power spectrum, $|D''(\omega)|^2$, in semicentral “132” reactions, for different Asy-EOS choices. The gamma multiplicity is simply related to it, see Eq.(6). The corresponding results for the stable “124” system are drawn in the right panel. As expected from the larger initial charge asymmetry, we clearly see an increase of the prompt dipole emission for the exotic n-rich beam. Such entrance channel effect allows also for a better observation of the Asy-EOS dependence. The asystiff case corresponds to a lower value of the centroid, ω_0 , and to a reduced total yield, as shown in figure 6. In fact, in the asystiff case we have a weaker restoring force for the dynamical dipole in the dilute “neck” region, where the symmetry energy is smaller [33], see figure 1. The sensitivity of ω_0 to the stiffness of the symmetry energy is more easily identified increasing $D(t_0)$, i.e. using exotic, more asymmetric beams. Moreover, a good sensitivity to the symmetry energy is also observed for dipole oscillations in more peripheral collisions [34], where low-density surface contributions become more important.

The pre-equilibrium dipole radiation angular distribution is the result of the interplay between the dinuclear rotation and the collective oscillation life-time. Since the latter is sensitive to the Asy-EOS, with a prompt dipole emission in the soft case, one also expects a sensitivity to the Asy-EOS of the anisotropy, in particular for high spin event selections [33].

4 Isospin equilibration and fragmentation mechanisms at Fermi energies

We now move to discuss reaction mechanisms occurring at the so-called Fermi energies (30-60 $AMeV$), where two-body correlations and fluctuations start to play an important role. In this energy range, reactions between charge asymmetric systems are characterized by a direct isospin transport in binary events (isospin diffusion). This process also involves the low density neck region and is sensitive to the low density behavior of E_{sym} , see Refs.[37,38] and references therein. Moreover, it is now quite well established that the largest part of the reaction cross section for dissipative collisions at Fermi energies goes through the *Neck*

Fragmentation channel, with intermediate mass fragments (IMF) directly produced in the interacting zone in semiperipheral collisions on short time scales [39]. It is possible to predict interesting isospin transport effects also for this fragmentation mechanism. Clusters are still formed in a dilute asymmetric matter but always in contact with the regions of the projectile-like and target-like remnants almost at normal densities, thus favoring the neutron enrichment of the neck region (isospin migration).

Results on these mechanisms, obtained with the SMF model, are discussed below. However, the main role of the isospin degree of freedom on the dynamics of a nuclear reaction can be easily understood, within the hydrodynamical limit, considering the behavior of neutron and proton chemical potentials as a function of density ρ and asymmetry $\beta = (N - Z)/A$ [40]. The *proton/neutron* currents can be expressed as

$$\mathbf{j}_{p/n} = D_{p/n}^\rho \nabla \rho - D_{p/n}^\beta \nabla \beta, \quad (7)$$

with $D_{p/n}^\rho$ the drift, and $D_{p/n}^\beta$ the diffusion coefficients for transport, which are given explicitly in Ref. [40]. Of interest for the study of isospin effects are the differences of currents between protons and neutrons which have a simple relation to the density dependence of the symmetry energy

$$\begin{aligned} D_n^\rho - D_p^\rho &\propto 4\beta \frac{\partial E_{sym}}{\partial \rho}, \\ D_n^\beta - D_p^\beta &\propto 4\rho E_{sym}. \end{aligned} \quad (8)$$

Thus the isospin transport due to density gradients (isospin migration) depends on the slope of the symmetry energy, or the symmetry pressure, while the transport due to isospin concentration gradients (isospin diffusion) depends on the absolute value of the symmetry energy. Hence transport phenomena in nuclear reactions appear directly linked to the EOS properties.

4.1 The isospin transport ratio

In peripheral and semi-peripheral reactions, it is interesting to look at the asymmetries of the various parts of the interacting system in the exit channel: emitted particles, projectile-like (PLF) and target-like fragments (TLF), and in the case of ternary (or higher multiplicity) events, IMF’s. In particular, one can study the so-called isospin transport ratio, which is defined as

$$R_{P,T}^x = \frac{2(x^M - x^{eq})}{(x^H - x^L)}, \quad (9)$$

with $x^{eq} = \frac{1}{2}(x^H + x^L)$. Here, x is an isospin sensitive quantity that has to be investigated with respect to equilibration. We consider primarily the asymmetry $\beta = (N - Z)/A$, but also other quantities, such as isoscaling coefficients, ratios of production of light fragments, etc. can be of interest [6,35,36]. The indices H and L refer to symmetric reactions between a heavy (n -rich) and a light (n -poor)

system, while M refers to the mixed reaction. P, T denote the rapidity region, in which this quantity is measured, in particular the PLF and TLF rapidity regions. Clearly, this ratio is ± 1 in the projectile and target regions, respectively, for complete transparency, and oppositely for complete rebound, while it is zero for complete equilibration.

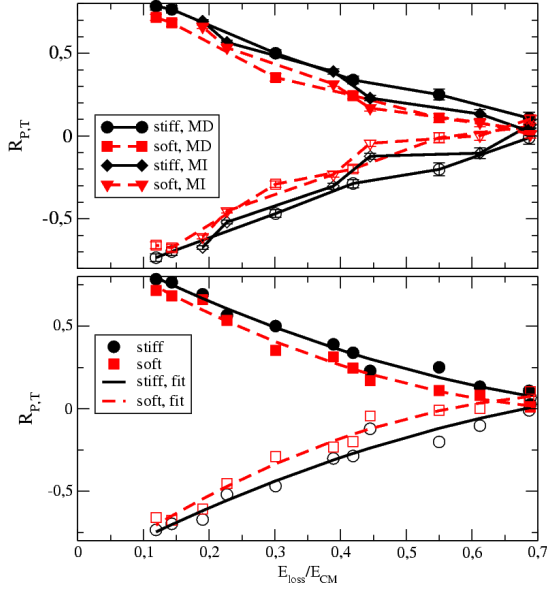


Fig. 7. Isospin transport ratios as a function of relative energy loss. Upper panel: separately for stiff (solid) and soft (dashed) Asy-EOS, and for two parameterizations of the isoscalar part of the interaction: MD (circles and squares) and MI (diamonds and triangles), in the projectile region (full symbols) and the target region (open symbols). Lower panel: quadratic fit to all points for the stiff (solid), resp. soft (dashed) Asy-EOS [38].

In a simple model one can show that the isospin transport ratio mainly depends on two quantities: the strength of the symmetry energy and the interaction time between the two reaction partners. Let us take, for instance, the asymmetry β of the PLF (or TLF) as the quantity x . At a first order approximation, in the mixed reaction this quantity relaxes towards its complete equilibration value, $\beta_{eq} = (\beta_H + \beta_L)/2$, as

$$\beta_{P,T}^M = \beta^{eq} + (\beta^{H,L} - \beta^{eq}) e^{-t/\tau}, \quad (10)$$

where t is the time elapsed while the reaction partners stay in contact (interaction time) and the damping τ is mainly connected to the strength of the symmetry energy [38]. Inserting this expression into Eq.(9), one obtains $R_{P,T}^\beta = \pm e^{-t/\tau}$ for the PLF and TLF regions, respectively. Hence the isospin transport ratio can be considered as a good observable to trace back the strength of the symmetry energy from the reaction dynamics provided a suitable selection of the interaction time is performed. The centrality dependence of the isospin ratio, for Sn + Sn collisions

at 35 and 50 $AMeV$, has been investigated in experiments as well as in theory [37,41,38,42]. Information about the stiffness of the symmetry energy, pointing to a L value in the region between 40 and 80 MeV (for a symmetry energy coefficient around 30 MeV at saturation) has been extracted from the analysis presented in [42], based on other transport models.

Here we investigate more in detail the relation between charge equilibration, interaction times and thermal equilibrium. Longer interaction times should be correlated to a larger dissipation and kinetic energy loss. It is then natural to look at the correlation between the isospin transport ratio and the total kinetic energy loss. In this way one can also better isolate the role of the symmetry energy in determining R from dynamical effects connected to the overall reaction dynamics (isoscalar effects), see [38]. In the calculations, we will employ two parametrizations of the isoscalar part of the nuclear interaction (one without momentum dependence, MI, see Eq.(3) and one with Momentum Dependence, MD, see [43,38]) and two symmetry energy parametrizations.

It is seen in figure 7 (top) that the curves for the asysoft EOS (dashed) are generally lower in the projectile region (and oppositely for the target region), i.e. show more equilibration, than those for the asystiff EOS, due to the higher value of the symmetry energy at low density. To emphasize this trend, all the values for the stiff (circles) and the soft (squares) Asy-EOS, corresponding to different impact parameters, beam energies and also to the two possible parametrizations of the isoscalar part of the nuclear interaction (MD and MI), are collected together in the bottom part of the figure. Though MD interactions lead to faster dynamics and shorter interaction times, one can see that, using the energy loss as a measure of the interaction time, all the points essentially follow a given line, depending only on the symmetry energy parameterization adopted. It should be noticed that in the MD calculations shown here the momentum dependence of the isovector channel of the effective interaction, leading to the splitting of neutron and proton effective masses, has been neglected. However, we have checked that the latter would modify the isospin transport ratio only by a few percent.

It is observed, that there is a systematic effect of the symmetry energy of the order of about 20 percent, which should be measurable. Moreover, we notice that the quantity R is a rapidly decreasing function of the degree of dissipation, E_{loss} , reached in the collision. This can be explained in terms of dissipation mechanisms mainly due to mean-field effects, as predicted by the SMF model. Indeed, according to a mean-field picture, a significant degree of thermal equilibrium (i.e. a considerable E_{loss}) implies a rather long contact time between the two reaction partners, thus certainly leading to isospin equilibration, which needs a short time scale to be reached. The correlation suggested in figure 7 should represent a general feature of isospin diffusion, expected on the basis of mean-field dominated mechanisms. On the other hand, when other dissipation mechanisms (like a sizable particle and fragment emission) become important, the energy loss is not

directly related to the interaction time between PLF and TLF and isospin equilibration may not occur even in very dissipative events. Thus it would be of great interest to verify experimentally the kind of correlations presented in figure 7. A similar analysis, exploiting the N/Z content of the light particle emission to extract the PLF asymmetry, has been performed in [44], pointing to a stiff behavior ($L \approx 75$ MeV) of the symmetry energy.

4.2 Isospin dynamics in neck fragmentation at Fermi energies

In presence of density gradients, as the ones occurring when a low-density neck region is formed between the two reaction partners in semi-peripheral collisions, the isospin transport is mainly ruled by the density derivative of the symmetry energy and so we expect a larger neutron flow to the neck clusters for a stiffer symmetry energy around saturation [5]. This mechanism leads to the neutron enrichment of the neck region (isospin migration). This effect is shown in figure 8, where the asymmetry of the neck and PLF-TLF regions, obtained in neutron-rich reactions at 50 $AMeV$, are plotted for two Asy-EOS choices.

From the experimental point of view, a new analysis has been recently published on Sn+Ni data at 35 $AMeV$ by the Chimera Collab.[45]. A strong correlation between neutron enrichment and fragment alignment (when the short emission time selection is enforced) is seen, that points to a stiff behavior of the symmetry energy ($L \approx 75$ MeV), for which a large neutron enrichment of neck fragments is seen (figure 8, top).

In order to build observables less affected by secondary decay effects, in figure 8 (bottom) we consider the ratio of the asymmetries of the IMF's to those of the residues (β_{res}) for stiff and soft Asy-EOS, as given by SMF results. This quantity can be roughly estimated on the basis of simple energy balance considerations. By imposing to get a maximum (negative) variation of E_{sym} when transferring the neutron richness from PLF and TLF towards the neck region, one obtains [38]:

$$\frac{\beta_{IMF}}{\beta_{res}} = \frac{E_{sym}(\rho_R)}{E_{sym}(\rho_I)} \quad (11)$$

From this simple argument the ratio between the IMF and residue asymmetries should depend only on symmetry energy properties and, in particular, on the different symmetry energy values corresponding to the residue and neck densities (ρ_R and ρ_I), as appropriate for isospin migration. It should also be larger than one, more so for the asystiff than for the asysoft EOS. It is seen indeed in figure 8 (bottom part), that this ratio is nicely dependent on the Asy-EOS only (being larger in the asystiff case) and not on the system considered. If final asymmetries were affected in the same way by secondary evaporation in the case of neck and PLF fragments, then one could directly compare the results of figure 8 (bottom) to data. However, due to the different size and temperature of the neck region with respect to PLF or TLF sources, de-excitation

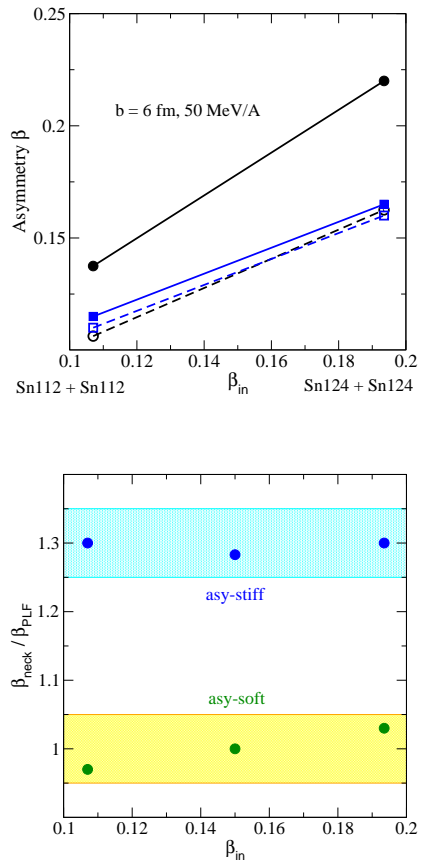


Fig. 8. Top panel: asymmetry of IMF's (circles) and PLF-TLF (squares), as a function of the system initial asymmetry, for two Asy-EOS choices: asystiff (full lines) and asysoft (dashed lines). Bottom panel: Ratio between the neck IMF and the PLF asymmetries, as a function of the system initial asymmetry. The bands indicate the uncertainty in the calculations [46].

effects should be carefully checked with the help of suitable decay codes.

4.3 Comparison with the predictions of different transport codes

A detailed investigation of isospin equilibration has been recently undertaken within transport codes based on the molecular dynamics (QMD) approach [42]. In comparison to the transport model considered before, mainly describing mean-field mechanisms (the SMF model, see Eq.(1)), such approaches, where nucleons are represented as individual wave packets of fixed compact shape (usually taken as gaussians), are well suited to describe fluctuations and correlations, especially in the exit channel of multi-fragmentation events, whereas some aspects of the mean-field dynamics may not be well accounted for. As shown in Ref.[42], where charge equilibration is investigated for $Sn+Sn$ reactions at 35 and 50 MeV/u , the ImQMD code predicts a quite different behavior with respect to SMF: the isospin transport ratio is rather flat as a function of

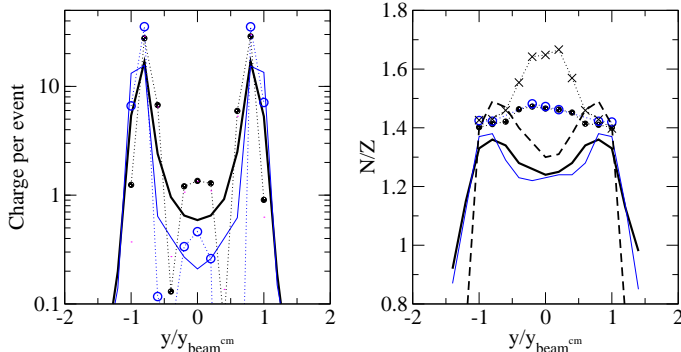


Fig. 9. Left panel: Average total charge per event, associated with IMF's, as a function of the reduced rapidity, obtained in the reaction $^{124}\text{Sn} + ^{124}\text{Sn}$ at 50 MeV/u. Results are shown for ImQMD calculations at $b = 6$ fm (thick line) and $b = 8$ fm (thin line) and for SMF calculations at $b = 6$ fm (full circles) and $b = 8$ fm (open circles). A soft interaction is considered for the symmetry energy. Right panel: N/Z of IMF's as a function of the reduced rapidity. Lines and symbols are like in the left panel. Results corresponding to a stiff Asy-EOS are also shown for ImQMD (dashed line) and SMF (crosses), for $b=6$ fm [46].

the impact parameter. This seems to indicate that, even in the case of central collisions, the contact time between the two reaction partners remains rather short, the dissipation mechanisms being mostly due to many-body correlations and particle emission, rather than to mean-field effects. Thus the more explosive dynamics could lead to the lower degree of isospin equilibration observed. It should be noticed that the stronger impact of many-body correlations on the fragmentation path in molecular dynamics approaches has also been evidenced, in the context of central collisions, performing a comparison between the predictions of the Antisymmetrized Molecular Dynamics (AMD) model and of the SMF approach [47].

To examine more in detail the origin of the observed discrepancies, results concerning IMF ($Z > 2$) properties, obtained with the SMF and ImQMD codes, are compared in figure 9. In the left panel, the average total charge per event, associated with IMF's, is plotted as a function of the reduced rapidity, for the reaction $^{124}\text{Sn} + ^{124}\text{Sn}$ at 50 MeV/u and impact parameters $b = 6$ and 8 fm. From this comparison it is clear that in ImQMD a larger number of light IMF's, distributed over all rapidity range between PLF and TLF, are produced. On the other hand, mostly binary or ternary events are observed in SMF, with light IMF's located very close to mid-rapidity. Then the different reaction dynamics predicted by the two codes may explain the different results seen for isospin equilibration especially in semi-peripheral and central reactions ($b \approx 4$ -6 fm). The fast ImQMD fragmentation dynamics inhibits nucleon exchange and charge equilibration, though the energy loss is rather large (due to cluster emission). On the

other hand, in SMF dissipation is dominated by mean-field mechanisms, acting over longer time intervals and leading to stronger equilibration effects.

Results on the neutron content of the neck region are illustrated in the right panel of figure 9, that shows the global N/Z of IMF's as a function of the reduced rapidity. As discussed above, SMF calculations clearly predict a larger N/Z for IMF's produced at mid-rapidity, with respect to PLF and TLF regions (isospin migration effect). The effect is particularly pronounced in the case of the asystiff parametrization. On the contrary, ImQMD calculations predict a minimum of the N/Z ratio at mid-rapidity. The reasons of these difference need to be further investigated. Moreover, it would be interesting to perform detailed comparisons with experimental data, also in consideration of the neck fragmentation analyses recently appeared in the literature [45].

5 Asy-EOS at supra-saturation density: collective flows

Reactions with neutron-rich systems at intermediate energies (100-500 $AMeV$) are of interest in order to have high momentum particles and to test regions of high baryon and isovector density during the reaction dynamics. In such a context, it is important to consider momentum dependent effective interactions, which essentially lead to the concept of effective masses. If also the isovector component of the interaction is momentum dependent, one observes different effective masses (i.e. effective mass splitting) for neutrons and protons. The problem of the precise determination of the Momentum Dependence in the Isovector channel ($Iso-MD$) of the nuclear interaction is still very controversial and it would be extremely important to get more definite experimental information [48, 49], looking at observables which may also be sensitive to the mass splitting.

Transport codes are usually implemented with different (n, p) momentum dependent interactions, see for instance [48, 49]. This allows one to follow the dynamical effect of opposite n/p effective mass (m^*) splitting while keeping the same density dependence of the symmetry energy [38].

Let us consider semicentral ($b/b_{max} = 0.5$) collisions of $^{197}\text{Au} + ^{197}\text{Au}$ at 400 $AMeV$ [50]. In the interacting zone baryon densities about $1.7 - 1.8\rho_0$ can be reached in a transient time of the order of 15-20 fm/c. The system is quickly expanding and the freeze-out time is around 50 fm/c. A rather abundant particle emission is observed over this time scale. Here it is very interesting to study again the collective response of the system. Collective flows are very good candidates since they are expected to be rather sensitive to the momentum dependence of the mean field, see [51, 5]. The transverse flow, $V_1(y, p_t) = \langle \frac{p_x}{p_t} \rangle$, where $p_t = \sqrt{p_x^2 + p_y^2}$ is the transverse momentum and y the rapidity along the beam direction, provides information on the anisotropy of nucleon emission on the reaction plane.

Very important for the reaction dynamics is also the elliptic flow, $V_2(y, p_t) = \langle \frac{p_x^2 - p_y^2}{p_t^2} \rangle$. The sign of V_2 indicates the azimuthal anisotropy of the emission: on the reaction plane ($V_2 > 0$) or out-of-plane (*squeeze-out*, $V_2 < 0$) [51].

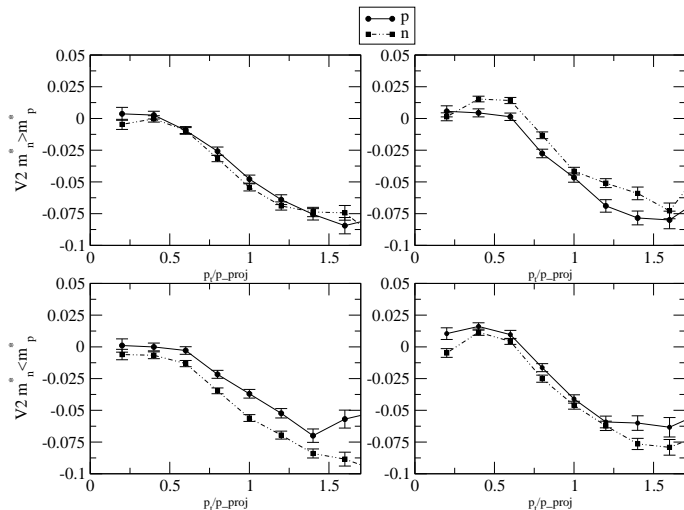


Fig. 10. Proton (thick) and neutron (thin) V_2 flows in a semi-central reaction Au+Au at 400 A MeV. Transverse momentum dependence at midrapidity, $|y_0| < 0.3$. Upper curves for $m_n^* > m_p^*$, lower curves for the opposite splitting $m_n^* < m_p^*$. Left: asystiff. Right: asysoft [50].

In figure 10, we plot the elliptic flow of emitted neutrons and protons, for different asy-stiffness and effective mass splitting choices. We are now exploring density regions above normal density. Therefore we expect a larger neutron repulsion in the asystiff case, corresponding to the larger symmetry energy value, see figure 1. Indeed in figure 10 we observe a larger (negative) squeeze-out for neutrons in the asystiff case (compare left and right panels). Moreover, the $m_n^* < m_p^*$ case will favor the neutron repulsion, leading to a larger squeeze-out for neutrons, compare top and bottom panels. In particular, in the asysoft case (on the right) we see an inversion of the neutron/proton squeeze-out at mid-rapidity for the two effective mass splittings.

Actually, we observe a rather interesting interplay between the effects linked to the symmetry energy and to the mass splitting: a larger (smaller) neutron effective mass may compensate the larger (smaller) neutron repulsion corresponding to the asystiff (asysoft) case. Indeed the $m_n^* < m_p^*$ case, with the soft Asy-EoS, yields very similar results of the $m_p^* < m_n^*$ case with the stiff Asy-EoS.

It seems to be difficult to conclude on the properties of the effective interaction (asystiffness and MD) just from the analysis of one single observable. However, coupling the flow information to the study of other observables, it would be possible to reach more definitive constraints of the effective interaction. For instance, in the considered beam energy range, the N/Z content of the particle

emission looks particularly sensitive just to the sign of mass splitting, rather than to the asy-stiffness [50]. Hence it would be very interesting to combine the information coming from particle flows and yields. Recent experimental analyses look very promising in this direction [52,53]. Due to the difficulties in measuring neutrons, one could also investigate the difference between light isobar (like ^3H vs. ^3He) flows and yields. We still expect to see effective mass splitting effects [50].

6 Hadron-Quark transition at high isospin and baryon density

In heavy ion collisions at beam energies in the AGeV range, rather high density regions can be reached, opening the possibility that new degrees of freedom come into play. This kind of collisions is usually described within relativistic mean-field (RMF) models and transport theories [5]. In neutron-rich systems, the transition from the nuclear (hadron) to the quark deconfined (quark-gluon plasma) phase could take place even at the density and temperature conditions reached along the collision dynamics. This kind of transition is also of large interest in the study of neutron stars.

At high temperature T and small quark chemical potential μ_q lattice-QCD calculations provide a valuable tool to describe such transition. The transition appears of continuous type (crossover) with a critical temperature T_c around 170-180 MeV. Isospin and other properties of the hadron interaction appear not relevant here.

However the fundamental lattice calculations suffer serious problems at large chemical potentials and the validity of the results at $\mu_q/T_c > 1$ is largely uncertain [54]. Some phenomenological effective models have been introduced, like the MIT-Bag [55] and the more sophisticated Nambu-Jona Lasinio (NJL) [56,57,58] and Polyakov-NJL [59,60,61] models, where the chiral and deconfinement dynamics is accounted for. We remark here that only scalar interactions are generally considered in the quark sector. The transition at low- μ is well in agreement with l-QCD results however still properties of the hadron sector are not included and so the expected transition at high baryon and isospin density cannot be trusted.

In order to overcome the problem and to get some predictions about the effect of the transition in compact stars [62,63,64,65,66,67,68] and high energy heavy ion collisions [69,70,71,72,73,74,75], recently Two-Phase (Two-Equation of State) models have been introduced where both hadron and quark degrees of freedom are considered, with particular attention to the transition in isospin asymmetric matter.

A simple argument can be used for the expected isospin effects. In figure 11 we report the energy per particle at $T = 0$ vs. the baryon density for the hadron (RMF EoS, [5]) and the quark (MIT-Bag) matter in the isospin symmetric ($\alpha_{H,Q} = 0$) and "pure neutron" ($\alpha_{H,Q} = 1$) cases. For energetic reasons we roughly expect the transition to appear around the crossings [71]. We see large isospin effects on the transition region: for symmetric matter we are

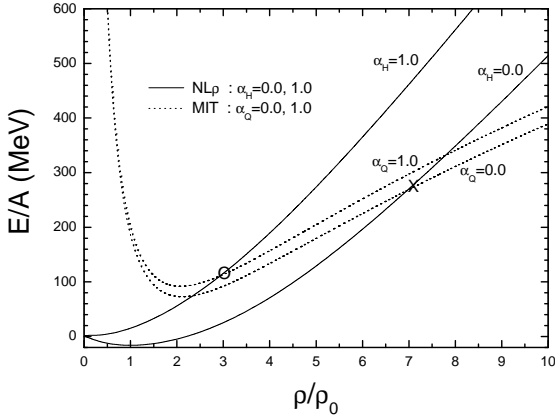


Fig. 11. (Color online) Energy per particle at zero temperature for the nucleon (solid) and quark (dotted) sectors for the cases of isospin symmetric ($\alpha = 0$) and "pure neutron" ($\alpha = 1$ matter) [71].

around 7 times the saturation density, for the completely isospin asymmetric matter we move down to $3\rho_0$. This is very interesting for neutron stars, as well as for heavy ion collisions in the $AGeV$ energy range. We note that this effect is due to the lower symmetry pressure in the quark phase, where the symmetry energy comes only from the kinetic Fermi contributions due to the lack of isovector interactions.

When a mixed (coexistence) phase of quarks and hadrons is considered, the Gibbs conditions (thermal, chemical and mechanical equilibrium)

$$\begin{aligned} \mu_B^H(\rho_B, \rho_3, T) &= \mu_B^Q(\rho_B, \rho_3, T) \\ \mu_3^H(\rho_B, \rho_3, T) &= \mu_3^Q(\rho_B, \rho_3, T) \\ P^H(\rho_B, \rho_3, T) &= P^Q(\rho_B, \rho_3, T), \end{aligned} \quad (12)$$

should be fulfilled [62]. In Eqs. (12), $\rho_B = (1 - \chi)\rho_B^H + \chi\rho_B^Q$ is the mean baryon density and $\rho_3 = (1 - \chi)\rho_3^H + \chi\rho_3^Q$ is the isospin density, where χ is the quark fraction. $\rho_B^{H,Q}/\rho_3^{H,Q}$, $\mu_B^{H,Q}/\mu_3^{H,Q}$ are baryon/isospin densities and corresponding chemical potentials in the two phases. $P^{H,Q}$ indicates the pressure in the two phases.

In heavy-ion collisions, for a given isospin asymmetry of the considered experiment, the global asymmetry parameter α

$$\alpha \equiv -\frac{\rho_3}{\rho_B} = -\frac{(1 - \chi)\rho_3^H + \chi\rho_3^Q}{(1 - \chi)\rho_B^H + \chi\rho_B^Q}, \quad (13)$$

keeps constant according to the isospin charge conservation in the strong interaction, but the local asymmetry parameters α^H, α^Q in the separate phases can vary with χ , which determines the energetically stable state of the system. For details, one can refer to Refs. [71, 74, 75].

In figures 12 and 13 we plot the phase transition curves with the Hadron-NJL and Hadron-PNJL models.

At low temperatures a clear earlier onset of the transition is observed for isospin asymmetric matter (see full lines of figure 13). For the NJL model with only chiral dynamics, no physical solution exists when the temperature is higher than ~ 80 MeV. The corresponding temperature is enhanced to about ~ 166 MeV with the Hadron-PNJL model, which is closer to the phase transition (crossover) temperature given by full lattice calculations at zero or small chemical potential. A general observation is that the coupling to the Polyakov loop field is essentially reducing the quark/antiquark distribution functions due to the confinement constraint. As a consequence the quark pressure at high temperature will be also reduced and this will make possible a hadron-quark first order transition at higher temperatures.

From figure 13 we remark that in both cases the region around the *Critical - End - Points* is almost not affected by isospin asymmetry contributions, which are relevant at lower temperatures and larger chemical potentials.

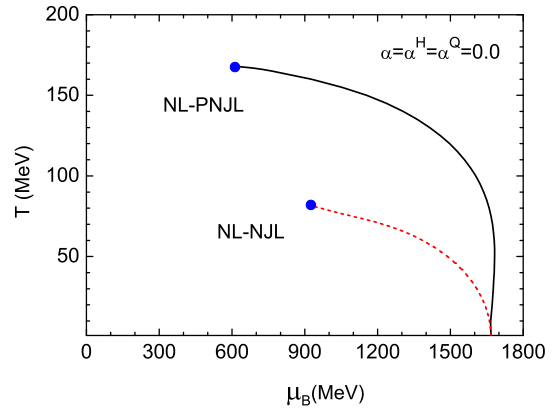


Fig. 12. (Color on line) Phase diagram in $T - \mu_B$ plane for symmetric matter [75].

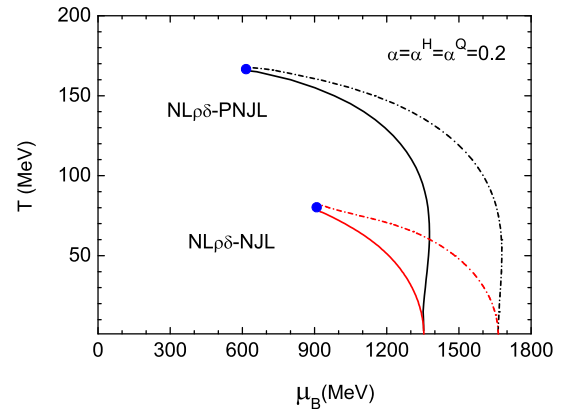


Fig. 13. (Color on line) Phase diagram in $T - \mu_B$ plane for asymmetric matter with the global asymmetry parameter $\alpha = 0.2$ [75].

For symmetric matter there is only one phase-transition line in the $T - \mu_B$ plane, i.e. the phase transition curve is independent of the quark fraction χ . At variance, for asymmetric matter, the phase transition curve varies for different quark fraction χ . The phase transition curves in figure 13 are obtained with $\chi = 0$ and 1, representing the beginning and the end of the hadron-quark transition, respectively. The reason is that we have an important Isospin Fractionation (Distillation) effect, i.e., an enhancement of the isospin asymmetry in the quark component inside the mixed phase, as reported in figure 14, where the asymmetry parameters in the two components are plotted vs. the quark fraction χ . In asymmetric matter at a fixed temperature, along the transition path, i.e. increasing the quark fraction, pressure and chemical potential change and the two coexisting phases have different asymmetry.

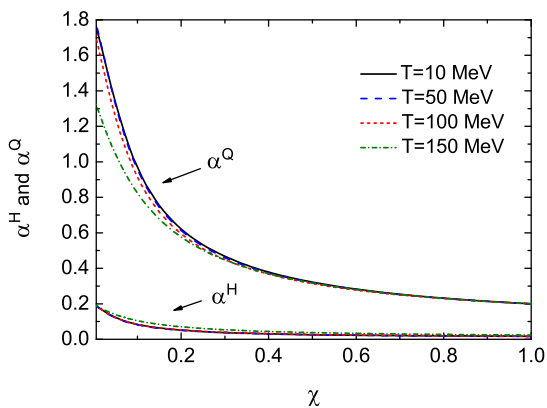


Fig. 14. (Color on line) The behavior of local asymmetric parameters α^H and α^Q in the mixed phase for several values of temperature. Parameter set $NL\rho\delta$ is used in the calculation [75].

These features of the local asymmetry may lead to some observable effects in the hadronization during the expansion phase of heavy ion collisions, such as an inversion in the trend of emission of neutron rich clusters, an enhancement of π^-/π^+ , K^0/K^+ yield ratios in high-density regions, as well as an enhancement of the production of isospin-rich resonances and subsequent decays, for more details see Refs. [71,74,75]. Such signals are possible to be probed in the newly planned facilities, such as FAIR at GSI-Darmstadt and NICA at JINR-Dubna.

6.1 Isoscalar vector quark interaction and existence of hybrid neutron stars

Inside this frame it appears natural to study the role of vector interactions in the quark effective models [76, 77]. We remind that in nuclear matter the vector interactions lead to fundamental properties, like the saturation point and the symmetry energy in isospin asymmetric systems. We discuss now the results obtained when the isoscalar-vector interaction channel in the quark sector is

turned on in the (P)NJL models. With increasing the ratio $R_V = G_\omega/G$ of the vector/scalar coupling constants, due to the repulsive contribution of the isoscalar-vector channel to the quark energy and, as a consequence, to the chemical potential, the phase-transition curves are moving towards higher values of density/chemical potential [77]. The larger repulsion in the quark phase is essential for the existence of massive hybrid neutron stars. The limit appears to be the impossibility of reaching the onset densities of the mixed phase in the inner core for large values of the vector coupling.

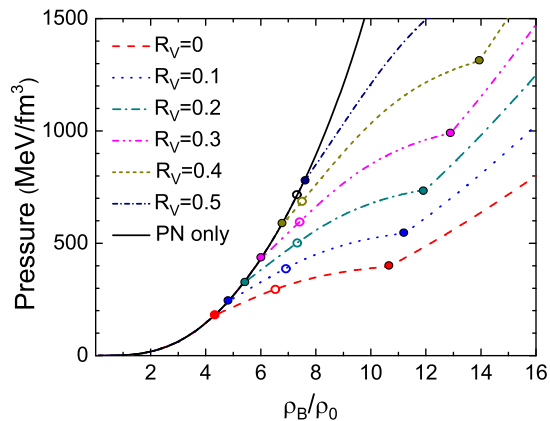


Fig. 15. (color on line) EoSs of neutron star matter without and with a hadron-quark phase transition for different isoscalar-vector interaction coupling G_V . For each value of R_V , the two solid dots with the same color indicate the range of the mixed phase, and the cycle marks the largest pressure that can be reached in the core of the neutron star [77].

We present in figure 15 the EoS of neutron star matter without (PN only) and with the hadron-quark phase transition for different strength of the isoscalar-vector interaction. For each value of $R_V = G_V/G$, the two solid dots with the same color indicate the range of the mixed phase, and the cycle marks the largest pressure that can be reached in the core of neutron star by solving the Tolman-Oppenheimer-Volkoff (TOV) equation. With increasing the vector strength in the quark sector the onset of the transition is moving to higher densities since the quark pressure is also increasing. A massive hybrid neutron star can be supported in the range 0.1-0.3 of the R_V ratio and good agreement with recent data for the Mass-Radius relation are also obtained [77].

7 Conclusions

We have reviewed some aspects of the rich phenomenology associated with heavy ion reactions, from which interesting hints are emerging to constrain the nuclear EOS and, in particular, the largely debated density behavior of the symmetry energy.

Information on the low density region can be accessed in reactions from low to Fermi energies, where collective

excitations and fragmentation mechanisms are dominant. Results on isospin sensitive observables have been presented. In particular, we have concentrated our analysis on the charge equilibration mechanism (and its relation to energy dissipation) and on the neutron-enrichment of the neck region in semi-peripheral reactions. From the study of the latter mechanisms, for which new experimental evidences have recently appeared [45,44], hints are emerging towards a moderately stiff behavior of the symmetry energy around normal density ($L \approx 75$ MeV). This is compatible with recent results from structure data, see for instance the review article [78]. We have also tried to address the problem of the model dependence of the results, suggesting possible ways to better ascertain, through the comparison with all available experimental observables, the overall reaction dynamics, thus increasing the robustness of the extracted symmetry energy information [47, 79, 80, 81].

The greatest theoretical uncertainties concerns the high density domain, that has the largest impact on the understanding of the properties of neutron stars. In particular, a large symmetry pressure would favor the onset of a quark phase in the inner core of neutron stars [77]. This regime can be explored in terrestrial laboratories by using intermediate energy and relativistic heavy ion collisions of charge asymmetric nuclei. Collective flows, cluster and meson production are promising observables. Moreover, if the mixed phase can be reached, at high baryon density, in collisions of isospin asymmetric heavy ions, an isospin fractionation effect, leading to a more asymmetric quark component, is expected to appear. Observable effects will be present in the subsequent hadronization.

A considerable amount of work has already been done in the symmetry energy domain. In the near future, thanks to the availability of both stable and rare isotope beams, more global analyses, also based on new sensitive observables, together with the comparison and the improvement of the available theoretical models, are expected to provide further stringent constraints.

Acknowledgements

We warmly thank G.Y. Shao for the fruitful collaboration, during his stay at LNS-Catania, on hadronic/quark matter phase transition and neutron star properties.

This work for V. Baran was supported by a grant of the Romanian National Authority for Scientific Research, CNCS - UEFISCDI, project number PN-II-ID-PCE-2011-3-0972.

References

1. P. Danielewicz, R. Lacey and W.G. Lynch, *Science* **298**, 1592 (2002).
2. J.M. Lattimer and M. Prakash, *Phys. Rep.* **442**, 109 (2007).
3. A. Carbone *et al*, *Phys. Rev. C* **81**, 041301 (2010).
4. *Isospin Physics in Heavy-ion Collisions at Intermediate Energies*, Eds. Li BA and Schröder WU, Nova Science Publishers (2001, New York)
5. V. Baran, M. Colonna, V. Greco and M. Di Toro, *Phys. Rep.* **410**, 335 (2005).
6. M. Colonna and M.B. Tsang, *Eur. Phys. Jou. A* **30**, 165 (2006), and references therein.
7. B.A. Li, L.W. Chen and C.M. Ko, *Phys. Rep.* **465**, 113 (2008).
8. P. Chomaz, M. Colonna and J. Randrup, *Phys. Rep.* **389**, 263 (2004).
9. M. Colonna *et al*, *Nucl. Phys. A* **642**, 449 (1998); J. Rizzo, Ph. Chomaz, M. Colonna, *Nucl. Phys. A* **806**, 40 (2008) and references therein.
10. A. Guarnera, M. Colonna, Ph. Chomaz, *Phys. Lett. B* **373** 267 (1996).
11. V. Baran, B. Frecus, M. Colonna and M. Di Toro, *Phys. Rev. C* **85**, 051601(R) (2012).
12. N. Paar, T. Nicsik, D. Vretenar, P. Ring, *Phys. Lett. B* **606**, 288 (2005).
13. A. Klimkiewicz *et al*, *Phys. Rev. C* **76**, 051603(R) (2007).
14. S. Yoshida, H. Sagawa, *Phys. Rev. C* **69**, 024318 (2004); *Phys. Rev. C* **73**, 044320 (2006).
15. J. Piekarewicz *Phys. Rev. C* **73**, 044325 (2006).
16. D. Savran *et al* *Phys. Rev. Lett.* **100**, 232501 (2008).
17. O. Wieland *et al* *Phys. Rev. Lett.* **102**, 092502 (2010); O. Wieland, A. Bracco, *Prog. Part. Nucl. Phys.* **66**, 304 (2011); H.K. Toft *et al*, *Phys. Rev. C* **81**, 064311 (2010).
18. A.P. Tonchev *et al*, *Phys. Rev. Lett.* **104**, 072501 (2010).
19. A. Makinaga *et al*, *Phys. Rev. C* **82**, 024314 (2010).
20. V. Baran, C. Rizzo, M. Colonna, M. Di Toro, D. Pierroussakou, *Phys. Rev. C* **79**, 021603(R) (2009).
21. X. Roca-Maza, G. Pozzi, M. Brenna, K. Mizuyama, G. Coló, *Phys. Rev. C* **85**, 024601 (2012).
22. M. Urban, *Phys. Rev. C* **85**, 034322 (2012).
23. V. Baran, M. Colonna, M. Di Toro, V. Greco, *Phys. Rev. Lett.* **86**, 4492 (2001); M. Colonna, P. Chomaz, S. Ayik, *Phys. Rev. Lett.* **88**, 122701 (2002).
24. E. Suraud, M. Pi, P. Schuck, *Nucl. Phys. A* **482**, 187c (1988).
25. V. Baran *et al*, arXiv:1306.4969
26. F. Calvayrac, P.G. Reinhard, E. Suraud, *Ann. Phys.* **225**, 125 (1997).
27. T. Inakura, T. Nakatsukasa, K. Yabana, *Phys. Rev. C* **84**, 021302(R) (2011).
28. P. Chomaz, M. Di Toro and A. Smerzi, *Nucl. Phys. A* **563**, 509 (1993).
29. D. Pierroussakou *et al*, *Phys. Rev. C* **71**, 054605 (2005).
30. B. Martin, D. Pierroussakou *et al* (Medea Collab.), *Phys. Lett. B* **664**, 47 (2008).
31. A. Sandulescu, M. Petrovici, A. Pop *et al*, *Jou. Phys. G* **7**, L55-L61 (1981).
32. V. Baran, D.M. Brink, M. Colonna and M. Di Toro, *Phys. Rev. Lett.* **87**, 182501 (2001).
33. V. Baran, C. Rizzo, M. Colonna, M. Di Toro and D. Pierroussakou, *Phys. Rev. C* **79**, 021603 (2009).
34. C. Rizzo *et al*, *Phys. Rev. C* **83**, 014604 (2011).
35. M. Colonna *et al*, *Phys. Rev. C* **78**, 064618 (2008).
36. M. Colonna, *Phys. Rev. Lett.* **110**, 042701 (2013)
37. M.B. Tsang *et al*, *Phys. Rev. Lett.* **92**, 062701 (2004).
38. J. Rizzo *et al*, *Nucl. Phys. A* **806**, 79 (2008).
39. M. Di Toro, A. Olmi and R. Roy, *Eur. Phys. Jou. A* **30**, 65 (2006).
40. V. Baran *et al*, *Phys. Rev. C* **72**, 064620 (2005).
41. Lie-Wen Chen, Che Ming Ko and Bao-An Li, *Phys. Rev. Lett.* **94**, 032701 (2005)

42. M.B. Tsang *et al*, Phys. Rev. Lett. **102**, 122701 (2009); Z.Y. Sun *et al*, Phys. Rev. C **82**, 051603 (2010).
43. C. Gale , G.F. Bertsch, S. Das Gupta, Phys.Rev. C **41**, 1545 (1990)
44. E. Galichet, M.Colonna, B.Borderie and M.F. Rivet, Phys. Rev. C **79**, 064615 (2009).
45. E. De Filippo *et al* (Chimera Collab.), Phys. Rev. C **86**, 014610 (2012).
46. M. Colonna *et al*, Jou. of Phys. Conference Series **420**, 012104 (2013)
47. M. Colonna, A. Ono, J. Rizzo, Phys. Rev. C **82**, 054613 (2010); J. Rizzo, M. Colonna, A. Ono, Phys. Rev. C **76**, 024611 (2007).
48. B.A. Li, B. Das Champak, S. Das Gupta and C. Gale, Nucl. Phys. A **735**, 563 (2004).
49. J. Rizzo, M. Colonna and M. Di Toro, Phys. Rev. C **72**, 064609 (2005).
50. V. Giordano *et al*, Phys. Rev. C **81**, 044611 (2010).
51. P. Danielewicz, Nucl. Phys. A **673**, 375 (2000).
52. P. Russotto *et al*, Phys. Lett. B **697**, 471 (2011).
53. M.D. Cozma, Phys. Lett. B **700**, 139 (2011).
54. K. Fukushima and T. Hatsuda, Rep. Prog. Phys. **74**, 014001 (2011).
55. A. Chodos *et al*, Phys. Rev. D **9**, 3471 (1974).
56. Y. Nambu and G. Jona-Lasinio, Phys. Rev. **112** (1961), 345; Phys. Rev. **124**, 246 (1961).
57. T. Hatsuda and T. Kunihiro, Phys. Rep. **247**, 221 (1994).
58. M. Buballa, Phys. Rep. **407**, 205 (2005).
59. K. Fukushima, Phys. Lett. B **591**, 277 (2004).
60. C. Ratti, M.A. Thaler, W. Weise, Phys. Rev. D **73**, 014019 (2006).
61. B.-J. Schaefer, M. Wagner, J. Wambach, Phys. Rev. D **81**, 074013 (2010).
62. N. K. Glendenning, Phys. Rev. D **46**, 1274 (1992).
63. N. K. Glendenning and J. Schaffner-Bielich, Phys. Rev. Lett. **81**, 4564 (1998); Phys. Rev. C **60**, 025803 (1999).
64. G. F. Burgio, M. Baldo, P. K. Sahu, and H.-J. Schulze, Phys. Rev. C **66**, 025802 (2002).
65. G. Y. Shao and Y. X. Liu, Phys. Rev. C **82**, 055801 (2010).
66. G. Y. Shao, Phys. Lett. B **704**, 343 (2011).
67. V. A. Dexheimer, S. Schramm, Phys. Rev. C **81**, 045201 (2010).
68. V. A. Dexheimer, S. Schramm, Nucl. Phys. B **199**, 319 (2010).
69. H. Müller, Nucl. Phys. A **618**, 349 (1997).
70. M. Di Toro, A. Drago, T. Gaitanos, V. Greco, and A. Lavagno, Nucl. Phys. A **775**, 102 (2006).
71. M. Di Toro *et al.*, Phys. Rev. C **83**, 014911 (2011).
72. B. Liu, M. Di Toro, G. Y. Shao, V. Greco, C. W. Shen, and Z. H. Li, Eur. Phys. J. A **47**, 104 (2011).
73. R. Cavagnoli, C. Providência, and D. P. Menezes, Phys. Rev. C **83**, 045201 (2011).
74. G. Y. Shao, M. Di Toro, B. Liu, M. Colonna, V. Greco, Y. X. Liu, and S. Plumari, Phys. Rev. D **83**, 094033 (2011).
75. G. Y. Shao, M. Di Toro, V. Greco, M. Colonna, S. Plumari, B. Liu, and Y. X. Liu, Phys. Rev. D **84**, 034028 (2011).
76. G. Y. Shao, M. Colonna, M. Di Toro, B. Liu, F. Matera, Phys. Rev. D **84**, 114017 (2012).
77. G. Y. Shao, M. Colonna, M. Di Toro, Y. X. Liu, B. Liu, Phys. Rev. D **87**, 096012 (2013).
78. M.B. Tsang *et al*, Phys. Rev. C **86**, 015803 (2012).
79. Z. Kohley, M. Colonna, A. Bonasera *et al*, Phys. Rev. C **85**, 064605 (2012).
80. D. Coupland *et al*, Phys. Rev. C **84**, 054603 (2011).
81. M.D. Cozma, Y. Leifels, W. Trautmann, Q. Li, P. Russotto, arXiv:1305.5417